第 35 卷第 11 期
2019 年 11 月

无 机 化 学 学 报
CHINESE JOURNAL OF INORGANIC CHEMISTRY

Vol.35 No.11
2117-2124

双功能镧系化合物:合成、结构、磁性和荧光性质

韩永芳[1,2] 蔡丽珍*,[1] 郭国聪*,[1]

([1]中国科学院福建物质结构研究所,结构化学国家重点实验室,福州 350002)

([2]中国科学院大学,北京 100039)

摘要:利用 *N*-succinopyridine(HL)配体,成功合成了 2 个同构型镧系化合物[$Ln(HL)_2(H_2O)_4$]Cl_3(Ln=Pr (**1**),Eu (**2**))并对其进行了结构表征。**1** 和 **2** 均由羧酸配体双桥联金属离子形成 1D 链结构,再通过氢键进一步相互连接构成了 3D 超分子结构。变温磁化率测试表明 **1** 中 Pr(Ⅲ)离子之间存在反铁磁相互作用,而在 **2** 中,Eu(Ⅲ)离子之间则表现出弱铁磁相互作用。固态发光测试观察到 **2** 可以发出很强的红光,但由于 Pr(Ⅲ)离子的能隙较大,未观察到 **1** 的特征峰。

关键词:镧系元素;*N*-琥珀酰吡啶;双功能化合物;磁性;发光

中图分类号:O614.33+4;O614.33+8;O611.2;O611.3 **文献标识码**:A **文章编号**:1001-4861(2019)11-2117-08

DOI:10.11862/CJIC.2019.229

Bi-functional Lanthanide Compounds: Synthesis, Structures, Magnetism and Fluorescence

HAN Yong-Fang[1,2] CAI Li-Zhen*,[1] GUO Guo-Cong*,[1]

([1]*State Key Laboratory of Structural Chemistry, Fujian Institute of Research on the Structure of Matter, Chinese Academy of Sciences, Fuzhou* 350002, *China*)

([2]*University of Chinese Academy of Sciences, Beijing* 100039, *China*)

Abstract: Two isostructural lanthanide (Ln) compounds with *N*-succinopyridine (HL) ligand, namely [$Ln(HL)_2(H_2O)_4$]Cl_3 (Ln=Pr (**1**), Eu (**2**)), have been synthesized and structurally characterized. Both **1** and **2** feature 1D chains with metal ions double-bridged by carboxyl ligands, which are further interconnected through hydrogen bonds to yield a 3D supramolecular architecture. Variable temperature magnetic susceptibility measurements revealed the presence of antiferromagnetic interaction between Pr(Ⅲ) ions for **1** but weak ferromagnetic interactions between Eu(Ⅲ) ions for **2**. Solid-state luminescence measurement showed that **2** emitted intense red luminescence, but no characteristic peak of **1** was observed due to the large energy gap of the Pr(Ⅲ) ion. CCDC: 885100, **1**; 902937, **2**.

Keywords: lanthanide; *N*-succinopyridine; bi-functional compound; magnetism; luminescence

0 Introduction

Bi-functional materials combining luminescence with magnetic properties have become a research focus due to their various applications, such as information storage, sensing (optical detection of magnetic compounds) and bio-imaging (combining for instance magnetic relaxation imaging (MRI) and fluorescence labelling)[1-3]. However, because of the quenching effect of paramagnetic transition metal (TM) ions on the luminescence of organic dyes, it is difficult to obtain magneto-optical materials from TM-based complexes[4].

收稿日期:2019-07-02。收修改稿日期:2019-09-17。

国家自然科学基金(No.91545201,21601185),中国科学院前沿科学重点研究计划(No.XDB20010000,QYZDB-SSW-SLH020),中国科学院青年创新促进会(No.2017J01033)和福建省自然科学基金(No.2018J01028)资助项目。

*通信联系人。E-mail:clz@fjirsm.ac.cn, gcguo@fjirsm.ac.cn

On the contrary, lanthanide-based complexes are well known for their magnetic properties with large angular momentum and crystal-field effect[5], as well as their exceptional luminescent properties with narrow band and long-lived emission, large Stokes shifts, high luminescence efficiency, and ligand-dependent luminescence sensitization[6-7]. In this regard, lanthanide ions have been incrementally used to design bi-functional magneto-optical materials by the rational choice of suitable ligands, which should hold not only efficient energy-transfer properties for the luminescent materials but also the proper orbitals for the construction of lanthanide-based magnetic materials[8-11].

Aromatic carboxylate ligands are usually used to construct lanthanide-based materials because carboxylic groups can clip fit well with the oxytropic lanthanide ions, and mediate strong magnetic interactions between paramagnetic centers[9]. Simultaneously, aromatic substituent groups can act as sensitive antennas to promote the luminescence of lanthanide ions and lead to π stacking[12-13]. Previously, we chose the *N*-succinylpyridine ligand to achieve two d^{10}-based compounds[14] and several lanthanide-based compounds[15], revealing the flexible coordination modes, rich fluorescent properties, and well magnetic mediums of *N*-succinylpyridine ligand. These results are very helpful for our further design and investigation on the bi-functional magneto-optical lanthanide-based materials.

In this work, we reported the preparation, structures, magnetic and fluorescent properties of two new complexes, $[Ln(HL)_2(H_2O)_4]Cl_3$ (Ln=Pr (**1**), Eu (**2**), HL=*N*-succinopyridine).

1 Experimental

1.1 Materials and instrumentation

N-succinopyridine was obtained according to the reported procedure[16], and other chemicals were commercially available analytical grade and used without further purification. The elemental analyses were carried out on an Elementar Vario EL Ⅲ microanalyzer 9. Powdered X-ray diffraction (PXRD) patterns were tested on a Rigaku MiniFlex Ⅱ diffractometer using Cu $K\alpha$ radiation (λ=0.154 2 nm) at 30 kV and 15 mA in a range of 5°~50°. The simulated patterns were finished by the Mercury software. The FT-IR spectra were measured on a Perkin-Elmer spectrum using KBr pellets as the matrices within 4 000~400 cm^{-1}. Optical diffuse reflectance spectra were achieved at room temperature on a PE Lambda 900 UV-Vis spectrophotometer used $BaSO_4$ plate as a standard (100% reflectance). Thermogravimetric analysis (TGA) experiments were recorded on a Netzsch STA449C-QMS403C thermogravimetric analyzer under N_2 atmosphere with the sample heated in an Al_2O_3 crucible at a heating rate of 10 $K\cdot min^{-1}$. The temperature dependence of magnetic susceptibility was done with a Quantum Design MPMS-XL superconducting quantum interference device (SQUID) magnetometer in a temperature range of 2~300 K at a field of 1 kOe and diamagnetic corrections were made using Pascal′s constants. The determination of PL was conducted on a double excitation monochromator Edinburgh FL920 fluorescence spectrometer equipped with a R928P PMT detector.

1.2 Syntheses of 1 and 2

The preparation procedures and methods of the two complexes are similar. The lanthanide halide (2 mmol) and *N*-succinylpyridine (195.2 mg, 1 mmol) were dissolved in 10.0 mL of distilled water and stirred under an atmosphere for 3 hours. Then the resulting solution was filtered into a glass beaker and slowly evaporated to crystallize. After about half a month, prismatic crystals which can be used for X-ray analysis were obtained. The crystal samples used for all testing and characterization were carefully hand-picked with the help of a microscope. The purity of the obtained crystalline samples was measured PXRD (Fig.1). Elemental analysis data of C, H, N was also used to prove the purity of test samples. Anal. Calcd. for $C_{18}H_{26}Cl_3N_2O_{12}Pr$ (**1**)(%): C, 30.44; H, 3.66; N, 3.95. Found(%): C, 29.31; H, 3.84; N, 3.74. Anal. Calcd. for $C_{18}H_{26}Cl_3N_2O_{12}Eu$ (**2**)(%): C, 29.97; H, 3.61; N, 3.89. Found(%): C, 29.39; H, 3.88; N, 3.60.

TG analysis data (Fig.2a) indicates that **1** and **2** are stable up to 109 and 114 ℃, then show a weight loss between 155 and 162 ℃, in accordance with the

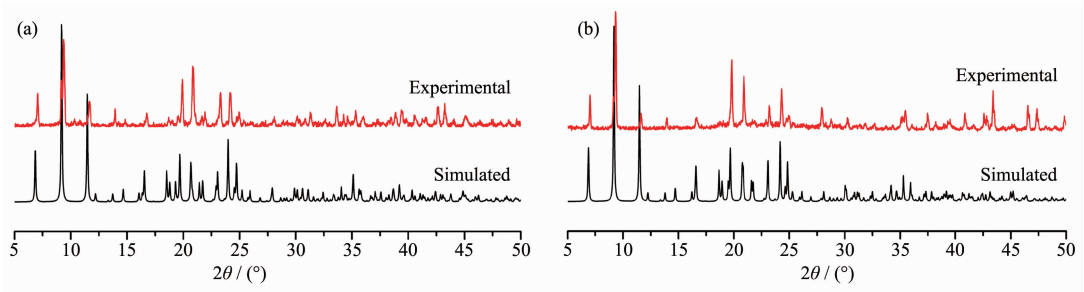

Fig.1　PXRD patterns of **1** (a) and **2** (b)

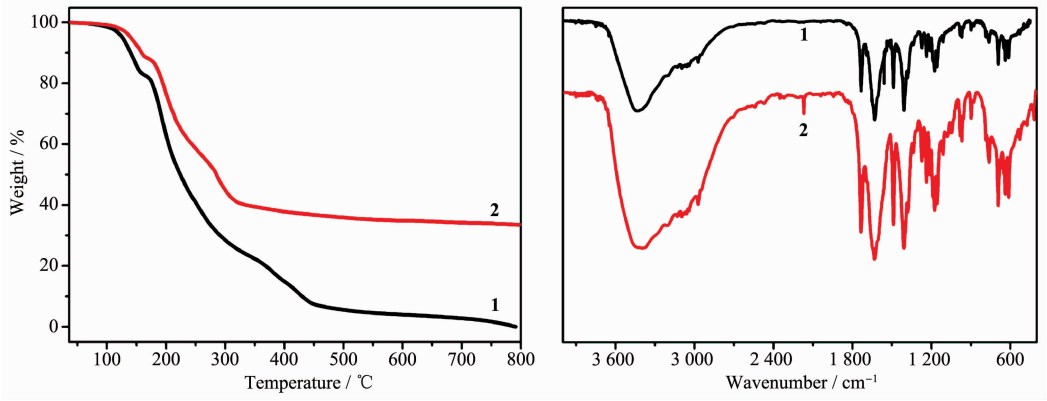

Fig.2　(a) TG curves of **1** and **2**; (b) IR spectra of **1** and **2**

removal of four coordinated water molecules (Obsd. 13.86% and 9.52%; Calcd. 10.15% and 10.00% for **1** and **2**, respectively). Yield based on HL: 49% for **1**; 18% for **2**. IR (KBr, cm^{-1}) (Fig.2b) for **1**: 3 430 (s), 1 735 (s), 1 632 (s), 1 559 (s), 1 488 (s), 1 409 (s), 1 272 (w), 1 238 (w), 1 210 (s), 1 175 (m), 1 159 (m), 1 109 (w), 984 (w), 971 (w), 896 (m), 785 (w), 764 (w), 694 (m), 637 (m), 613 (m); **2**: 3 447~3 393 (s), 1 737 (s), 1 630 (s), 1 489 (s), 1 409 (s), 1 338 (m), 1 274 (m), 1 238 (m), 1 177 (s), 1 156 (s), 1 111 (m), 1 082 (m), 1 050 (m), 984 (m), 969 (m), 899 (w), 764 (m), 693 (s), 640 (m), 613 (s), 529 (m), 477 (w), 420 (w).

1.3　Single-crystal diffraction analysis

The single-crystal X-ray diffraction measurement was collected on a Rigaku AFC7R diffractometer for **1** and Rigaku SCX mini for **2**, respectively, which were equipped with Mo $K\alpha$ radiation (λ =0.071 07 nm). Evidence during data collection indicated that the crystal did not decay, indicating that the obtained polymers were stable at ambient temperature. The intensity data sets were collected with the ω scan technique and corrected for Lp effects. The primitive structures were solved by the direct method and reduced by the CrystalClear software[17]. The subsequent successive difference Fourier syntheses yielded the other non-hydrogen atoms. The final structure was refined using a fullmatrix least-squares refinement on F^2. All non-hydrogen atoms were refined anisotropically. The hydrogen atoms of HL molecule were added geometrically and refined using the riding model. The hydrogen atoms of all water molecules were located in the idealized positions and refined with O-H distances restrained to a target value of 0.085 nm, the H-H distance to 0.134 nm, and $U_{iso}(H)=1.5U_{eq}(O)$. All of the calculations were performed by the Siemens SHELXTL version 5 package of crystallographic software[18]. The crystal data and structure refinement results for **1** and **2** are given in Table 1. The selected bond lengths (nm) and angles (°) are given in Table 2 and Table 3.

CCDC: 885100, **1**; 902937, **2**.

2　Results and discussion

2.1　Crystal structure description

The single-crystal X-ray diffraction analyses indicated that **1** and **2** belong to isostructural phases. Hence, compound **1** is taken as an example to depict

Table 1 Crystal and structure refinement data for 1 and 2

Compound	1	2
Formula	$C_{18}H_{26}Cl_3N_2O_{12}Pr$	$C_{18}H_{26}Cl_3N_2O_{12}Eu$
Formula weight	709.67	720.72
Crystal system	Monoclinic	Monoclinic
Space group	*P*2/*c*	*P*2/*c*
a / nm	1.308 2(6)	1.301 2(5)
b / nm	0.961 9(5)	0.962 7(4)
c / nm	1.119 2(5)	1.108 2(4)
β / (°)	99.73(4)	99.563(6)
V / nm^3	1.388 0(11)	1.368 8(9)
Z	2	2
D_c / (g·cm^{-3})	1.698	1.749
μ / mm^{-1}	2.102	2.643
Parameter, restraint, data	187, 7, 2 187	179, 0, 2 163
R_1[a] [$I>2\sigma(I)$]	0.031 8	0.042 8
wR_2[b] [$I>2\sigma(I)$]	0.082 5	0.112 1
Goodness of fit	1.007	1.069

[a] $R_1=\sum(F_o-F_c)/\sum F_o$; [b] $wR_2=[\sum w(F_o^2-F_c^2)^2/\sum w(F_o^2)^2]^{1/2}$.

Table 2 Selected bond lengths (nm) and angles (°) for 1

Pr(1)-O(1)	0.242 7(3)	Pr(1)-O(2)#1	0.237 8(3)	Pr(1)-O(1W)	0.251 4(3)
Pr(1)-O(2W)	0.252 5(4)				
O(2)#1-Pr(1)-O(1)#3	86.52(11)	O(1)#3-Pr(1)-O(1)	147.12(18)	O(1W)#3-Pr(1)-O(1W)	68.65(17)
O(1)-Pr(1)-O(1W)	72.67(12)	O(2W)-Pr(1)-O(2W)#3	79.56(18)	O(2)#2-Pr(1)-O(1W)#3	75.14(13)

Symmetry codes: #1: *x*, −*y*+1, *z*+1/2; #2: −*x*+1, −*y*+1, −*z*+2; #3: −*x*+1, *y*, −*z*+5/2.

Table 3 Selected bond lengths (nm) and angles (°) for 2

Eu(1)-O(2)	0.233 1(4)	Eu(1)-O(1W)	0.247 5(4)	Eu(1)-O(2W)	0.247 6(4)
Eu(1)-O(1)#2	0.237 5(4)				
O(2)-Eu(1)-O(1)#3	86.21(15)	O(1)#2-Eu(1)-O(2W)	140.28(15)	O(1)#2-Eu(1)-O(1)#3	146.8(2)
O(2)#1-Eu(1)-O(2W)#1	77.59(15)	O(1W)-Eu(1)-O(1W)#1	78.0(2)	O(1)#3-Eu(1)-O(2W)	72.67(15)

Symmetry codes: #1: −*x*+1, *y*, −*z*+3/2; #2: *x*, −*y*+1, *z*−1/2; #3: −*x*+1, −*y*+1, −*z*+2.

the crystal structure. Compound **1** crystallizes in the monoclinic system *P*2/*c*. (No.147), and the asymmetric unit consists of one Pr(Ⅲ) ion, one neutral HL ligand, two coordinated water molecules, one and half a Cl^- anions.

As shown in Fig.3a, every Pr(Ⅲ) ion coordinates eight oxygen atoms and exhibits distorted square anti-prismatic geometry. One basal aspect of the reverse prism composes of O1, O1W, O2#2 and O2W atoms, and the other base builds up with O2W#3, O2#1, O1#3 and O1W#3 atoms. The Pr-O bond distances ranging from 0.237 8(3) to 0.252 5(4) nm are normal as compared with Pr carboxylates[15,19-21]. Note that Cl2 atom splits up into Cl2 and Cl21 with the SOF value of 0.35(0) and 0.15(0). Adjacent Pr(Ⅲ) ions are doubly bridged by syn-syn carboxylate groups forming linear 1D chains. Neighboring chains form 2D layered structure by O3⋯Cl1⋯O1W hydrogen bonds along *b* axis (Fig.3b). Finally, these layers are further expanded into a 3D network through the hydrogen

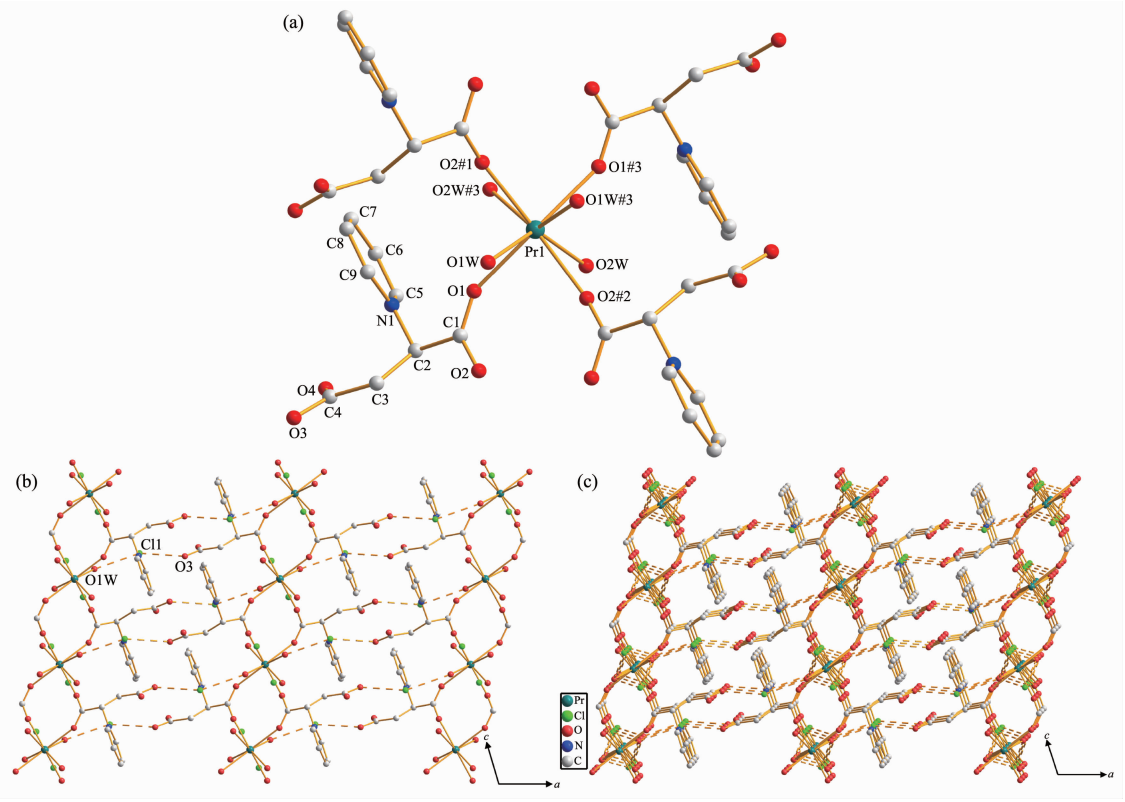

Symmetry codes: #1: x, $-y+1$, $z+1/2$; #2: $-x+1$, $-y+1$, $-z+2$; #3: $-x+1$, y, $-z+5/2$

Fig.3　(a) Coordination environment of Pr(Ⅲ) in **1**; (b) View of the hydrogen bonding 2D framework of **1** along b axis; (c) View of the hydrogen bonding 3D framework of **1** along b axis

bonding of O1W⋯Cl2⋯O2W　(O3⋯Cl1 0.304 0(4) nm, Cl1⋯O1W 0.306 3(5) nm, O1W⋯Cl2 0.314 5(5) nm, Cl2⋯O2W 0.313 5(5) nm, Fig.3c). The coordination mode of ligand in **1** is different to that in our previous work[15], revealing the flexible coordination modes of HL. The intrachain distance of Pr⋯Pr is 0.564 0(2) nm and the nearest interchain distance of Pr⋯Pr is 0.961 9(5) nm. It is worth noting that although the lanthanide ions has a good affinity for oxygen, only one carboxylate unit is coordinated to Pr(Ⅲ) ions in the HL ligand.

2.2　Magnetic properties

2.2.1　Magnetic property of **1**

The temperature dependence of magnetic susceptibility for **1** is investigated and presented in Fig.4. Compound **1** exhibited a $\chi_M T$ value of 1.62 $cm^3 \cdot K \cdot mol^{-1}$ at room temperature, which is in excellent agreement with the theoretical value of 1.60 $cm^3 \cdot K \cdot mol^{-1}$ for an uncoupled Pr(Ⅲ) ion ($^3H_4$, g=4/5) in the ground state. As the temperature was lowered from 300 to 2 K, the $\chi_M T$ value decreased gradually and reached a minimum of 0.08 $cm^3 \cdot K \cdot mol^{-1}$, which could be caused by a selective depopulation of the excited crystal field state and antiferromagnetic interaction between Pr(Ⅲ) ions. There are no available expressions to estimate the magnetic susceptibility because of the large anisotropy in this 1D system. In order to get a rough quantitative estimation of the magnetic interaction between Pr(Ⅲ) ions, it can be assumed that the Pr(Ⅲ) ion exhibits a splitting of the m_j energy

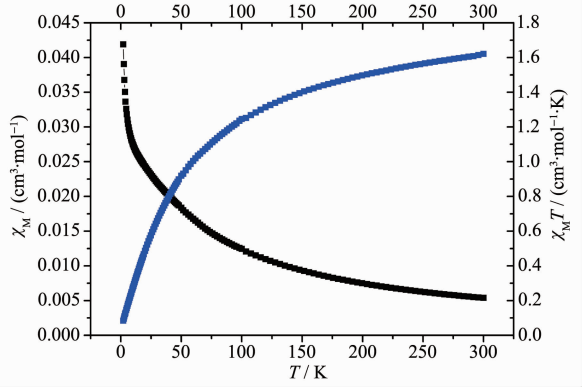

Fig.4　Plots of $\chi_M T$ and χ_M vs T for **1**

levels ($\hat{H}=\Delta\hat{J}_z^2$) in an axial crystal field. Therefore, χ_{Pr} and χ_M can be described as equation (**1**) and (**2**), respectively.

$$\chi_{Pr}=Ng^2\beta^2[2e^{-\Delta/(kT)}+8e^{-4\Delta/(kT)}+18e^{-9\Delta/(kT)}+32e^{-16\Delta/(kT)}]/\{kT[1+2e^{-\Delta/(kT)}+2e^{-4\Delta/(kT)}+2e^{-9\Delta/(kT)}+2e^{-16\Delta/(kT)}]\} \quad (1)$$

$$\chi_M=\chi_{Pr}/\{1-[2zJ'/(Ng^2\beta^2)]\chi_{Pr}\} \quad (2)$$

In these formulas, Δ is the zero-field splitting parameter, and N, g, β, and k represent their basic meanings. By using the above equation and considering the molecular field approximation with zJ' as the total exchange parameter between Pr(Ⅲ) ions, we can fit our experimental data with Eq.(**2**). The best fitting of the susceptibility data in a temperature range of 8~300 K gave zJ'=−2.71 cm^{-1}, Δ=0.99 cm^{-1}, g=0.89, and $R=\sum(\chi_{obsd}-\chi'_{cacld})^2/\sum(\chi_{obsd})^2=1.82\times10^{-4}$. The negative value of zJ' demonstrates that an overall antiferromagnetic interaction between Pr(Ⅲ) ions is operative.

2.2.2 Magnetic property of **2**

About Eu(Ⅲ), due to the weak energy separation and spin-orbit coupling, the crystal field effects and the possible thermal population of higher states should be accounted. The χ_MT and χ_M vs T plots for **2** are shown in Fig.5. **2** had a χ_MT value of 1.29 cm^3·K·mol^{-1}, which is much higher than the expected value of 0 cm^3·K·mol^{-1} for one isolated Eu(Ⅲ) ion in the ground state. Upon cooling, χ_MT gradually reached a value close to zero (0.016 cm^3·K·mol^{-1}) at 2 K because of the depopulation of Stake levels, which corresponds to a nonmagnetic ground state of $^7F_0$ for Eu(Ⅲ) ions. The shape of the curve is a typical characteristic occurrence of thermally populated excited states. As for Eu(Ⅲ), the ^7F ground term is split by the spin-orbit coupling ($\hat{H}=\lambda LS$) into seven states ^7F_J, with J ranging from 0 to 6. The $^7F_0$ ground state is taken as the origin, and λ is small enough for the first excited states to be thermally populated (around 300 cm^{-1}), the magnetic susceptibility follows the numerical expression given in Eq.(**3**):

$$\chi_M=AN\beta^2/[3Bkx(T-\theta)] \quad (3)$$

with $A=24+[(27x-3)/2]e^{-x}+[(135x-5)/2]e^{-3x}+(189x-7/2)e^{-6x}+(405x-9/2)e^{-10x}+[(1\,485x-11)/2]e^{-15x}+[(2\,457x-13)/2]e^{-21x}$ and $B=1+3e^{-x}+5e^{-3x}+7e^{-6x}+9e^{-10x}+11e^{-15x}+13e^{-21x}$ and where N stands for Avogadro's number, β for the Bohr magneton, k the Boltzmann constant, T the temperature, θ the Weiss constant, $x=\lambda/(kT)$ and λ the spin-orbit coupling parameter. The best fitting of the χ_MT vs T curve in a temperature range of 20~300 K gave the spin-coupling parameter, λ=373 cm^{-1}, a value in the expected range, and θ=3.17 K, R^2=0.999 41. The positive θ value reveals the presence of weak ferromagnetic interactions between Eu(Ⅲ) ions.

2.3 Optical properties

The reflectance diffusion spectra (Fig.6) reveals that **1** and **2** display intense π-π* transition absorption bands at 274 and 285 nm, respectively. In addition, the characteristic f-f electronic transition bands at 444, 470, 482, and 594 nm attributed to $^3H_4\rightarrow{}^3P_J$ (J= 2, 1, 0) and $^1D_2$ for Pr(Ⅲ) ion in **1**, 318 nm ($^7F_0\rightarrow{}^5H_5$), 363 nm ($^7F_0\rightarrow{}^5D_4$), 375 nm ($^7F_0\rightarrow{}^5G_4$), 383 nm ($^7F_0\rightarrow{}^5G_3$), 393 nm ($^7F_0\rightarrow{}^5L_6$), 465 nm ($^7F_0\rightarrow{}^5D_2$), 525 nm ($^7F_0\rightarrow{}^5D_1$), 534 nm ($^7F_1\rightarrow{}^5D_1$) for Eu(Ⅲ) ion in **2** were also observed.

The solid-state luminescence properties of these two complexes are also investigated at room

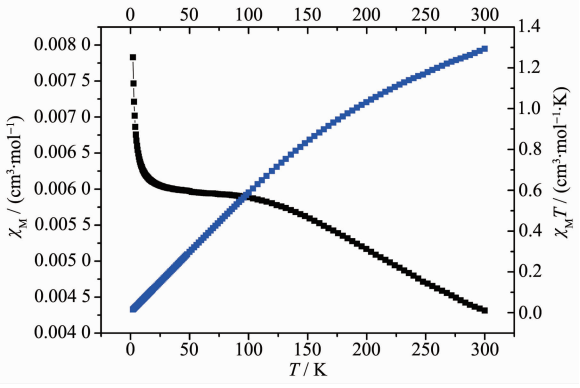

Fig.5 Plots of χ_MT and χ_M vs T for **2**

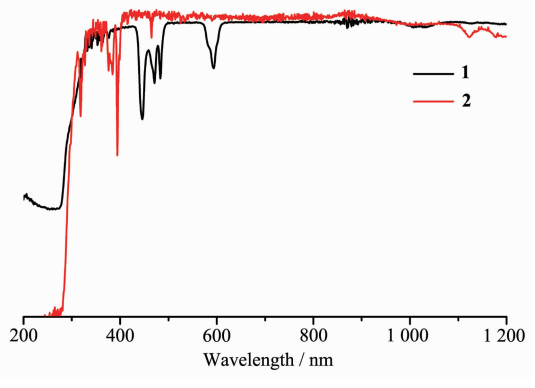

Fig.6 Optical diffuse reflectance spectra of **1** and **2**

temperature. Upon excitation at 396 nm, **2** emitted intense red luminescence (Fig.7) and exhibited four characteristic peaks at 590, 612, 650, and 697 nm, respectively, corresponding to the transitions of Eu(Ⅲ) from $^5D_0$ to ^7F_J (J=1, 2, 3 and 4). The quite weak emission band for $^5D_0 \rightarrow {}^7F_0$ in the position of 575 nm is due to the symmetry-forbidden transition of the Eu(Ⅲ) ion in **2**. It is well known that the $^5D_0 \rightarrow {}^7F_1$ transition is magnetic dipole in nature and less sensitive to its environment, while $^5D_0 \rightarrow {}^7F_2$ is electric dipole in origin and its intensity is strongly influenced by the crystal field[22-23]. The intensity ratio of $D_0 \rightarrow {}^7F_2$ to $^5D_0 \rightarrow {}^7F_1$ is about 2.5, implying relatively low-symmetric crystal field for the center Eu(Ⅲ) in **2**, which is consistent with the single-crystal structure. Luminescence lifetime measurements in solid monitored at 614 nm of **2** was 0.233 ms. Regrettably, because of the large energy gap of the Pr(Ⅲ) ion, no characteristic peak for Pr(Ⅲ) ion was observed in the luminescent spectra of **1**. These results suggest that energy transfer from the ligands to the resonance level of lanthanide ions is efficient for Eu(Ⅲ) ion but not for Pr(Ⅲ) ion.

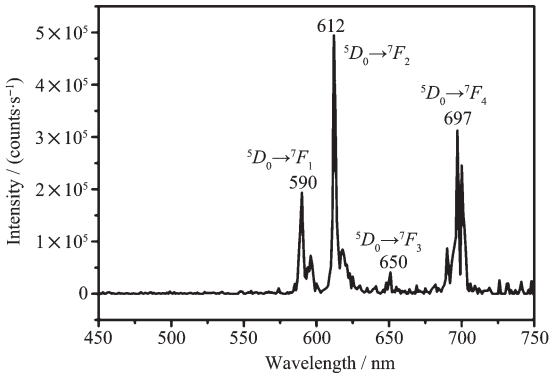

Fig.7　Solid-state emission spectra of **2** at room temperature

3　Conclusions

In conclusion, two new 3D isostructural polymers based on *N*-succinopyridine ligand have been synthesized in aqueous solution at room temperature and characterized in terms of structure, magnetic properties and luminescence. The magnetic studies show that the $\chi_M T$ value of **1** decreases as the temperature drops, which could arise from a selective depopulation of the excited crystal field state and antiferromagnetic interaction between Pr(Ⅲ) ions. And **2** is a typical characteristic occurrence of thermally populated excited states because of the weak energy separation and spin-orbit coupling. The efficient energy transfer from the HL ligand to the resonance level of lanthanide ions results in that **2** exhibited intense characteristic luminescent property of Eu(Ⅲ).

Conflicts of interest: There are no conflicts to declare.

Acknowledgements: This work was financially supported by the National Natural Science Foundation of China (Grants No. 91545201, 21601185), the Key Research Program of Frontier Sciences, CAS (Grants No.XDB20010000, QYZDB-SSW-SLH020), the Youth Innovation Promotion Association of CAS, the Natural Science Foundation of Fujian Province (Grants No.2017J01033, 2018J01028).

References:

[1] Bi Y, Wang X T, Liao W, et al. *Inorg. Chem.*, **2009**,**48**(24): 11743-11747

[2] Cucinotta G, Perfetti M, Luzon J, et al. *Angew. Chem. Int. Ed.*, **2012**,**51**(7):1606-1610

[3] Bi Y, Chen C, Zhao Y F, et al. *Chem. Sci.*, **2016**,**7**(8):5020-5031

[4] Long J, Guari Y, Ferreira R A S, et al. *Coord. Chem. Rev.*, **2018**,**363**:57-70

[5] Liddle S T, Slageren J J. *Chem. Soc. Rev.*, **2015**,**44**(19):6655-6669

[6] Eliseeva S V, Bunzli J C. *Chem. Soc. Rev.*, **2010**,**39**(1):189-227

[7] Bunzli J C. *Chem. Rev.*, **2010**,**110**(5):2729-2755

[8] Pointillart F, Guennic B L, Cador O, et al. *Acc. Chem. Res.*, **2015**,**48**(11):2834-2842

[9] Pointillart F, Cador O, Guennic B L, et al. *Coord. Chem. Rev.*, **2017**,**346**:150-175

[10]Hareri M A, Gavey E L, Regier J, et al. *Chem. Commun.*, **2016**,**52**(76):11335-11338

[11]Long J, Rouquette J, Thibaud J M, et al. *Angew. Chem. Int. Ed.*, **2015**,**54**(7):2236-2240

[12]Guillou O, Daiguebonne C, Calvez G, et al. *Acc. Chem. Res.*, **2016**,**49**(5):844-856

[13]Wu J W, Zhang H B, Du S W. *J. Mater. Chem. C*, **2016**,**4**(16):3364-3374

[14]Cai L Z, Wang M S, Zhang M J, et al. *CrystEngComm*, **2012**, **14**(19):6196-6200

[15]Cai L Z, Wang M S, Wang S H, et al. *CrystEngComm*, **2013**, **15**(38):7670-7679

[16]Kotov V Y, Gorbunova Y G, Kostina S A, et al. *Mendeleev Commun.*, **2001**,**11**(5):181-182

[17]*CrystalClear, Ver.* 1.35, *Software User's Guide for the Rigaku R-Axis, and Mercury and Jupiter CCD Automated X-ray Imaging System*, Rigaku Molecular Structure Corporation: UT, **2002**.

[18]*SHELXTL Reference Manual, Ver.* 5, Siemens Energy & Automation Inc.: Madison, WI, **1994**.

[19]Chen F, Wang J, Dong M W, et al. *J. Mol. Struct.*, **2019**, **1177**:117-123

[20]Yuan G, Zhang C, Shao K Z, et al. *Inorg. Chem. Commun.*, **2019**,**99**:126-130

[21]Wang Y, Xing S H, Bai F Y, et al. *Inorg. Chem.*, **2018**,**57**(20):12850-12859

[22]Zhou X, Wang H, Jiang S, et al. *Inorg. Chem.*, **2019**,**58**(6):3780-3788

[23]Wang Z X, Wu Q F, Liu H J, et al. *CrystEngComm*, **2010**, **12**(4):1139-1146